

# Highly dispersed Cu atoms in MOF-derived N-doped porous carbon inducing Pt loads for superior oxygen reduction and hydrogen evolution

Chao Wang<sup>a</sup>, Long Kuai<sup>\*,b</sup>, Wei Cao<sup>c</sup>, Harishchandra Singh<sup>c</sup>, Alexei Zakharov<sup>d</sup>, Yuran Niu<sup>d</sup>, Hongxia Sun<sup>a</sup> and Baoyou Geng<sup>\*,a,d</sup>

<sup>a</sup>College of Chemistry and Materials Science, The key Laboratory of Functional Molecular Solids, Ministry of Education, The Key Laboratory of Electrochemical Clean Energy of Anhui Higher Education Institutes, Anhui Provincial Engineering Laboratory for New-Energy Vehicle Battery Energy-Storage Materials, Anhui Normal University, Wuhu, 241002, China.

<sup>b</sup>School of Chemical and Environmental Engineering, Anhui Polytechnic University

<sup>c</sup>Nano and Molecular Systems Research Unit, University of Oulu, FIN-90014, Finland.

<sup>d</sup>MAX IV Laboratory, Lund University, P.O. Box 118, 22100 Lund, Sweden.

<sup>e</sup>Institute of Energy, Hefei Comprehensive National Science Center, Anhui, Hefei, 230031, China.

Corresponding Author:

Email: [kuailong@ahpu.edu.cn](mailto:kuailong@ahpu.edu.cn) (Long Kuai); [bygeng@mail.ahnu.edu.cn](mailto:bygeng@mail.ahnu.edu.cn) (Baoyou Geng)

## Abstract

The preparation of oxygen reduction reaction (ORR) and hydrogen evolution reaction (HER) catalysts with high activity, stability and low platinum loading has always

been the focus of research. The single-atom platinum supported catalyst greatly improves the utilization of platinum, but the catalytic activity and selectivity are greatly affected by the platinum coordination environment, and the preparation of the material is difficult. Doping base metals to adjust the electronic structure of platinum is an effective strategy to improve catalyst performance. In this work, copper-platinum alloy nanoparticles were loaded on N-doped porous carbon via a targeted route guided by highly dispersed Cu atoms derived from MOF. The product C-ZIF-CuPt has high activity and high stability ORR, HER bifunctional catalytic performance, which is better than commercial Pt/C (20 wt %). The Pt activity in C-ZIF-CuPt is 4.4 times (ORR) and 6.7 times (HER) than Pt/C. Spectromicroscopic determinations unveiled that strong interactions between carbon carrier and the CuPt alloys contribute to the overall stabilities. DFT calculations show that Cu doping can increase the d-band center of Pt, reduce the ORR overpotential, and the activation energy barrier to water molecules, which is beneficial to ORR and HER catalysis. Under the same carrier conditions, the performance of sub-nano (single atoms, clusters) platinum-supported catalysts (C-ZIF-Cu-Pt) is inferior to C-ZIF-CuPt. This further shows that platinum alloying can effectively improve the performance of the catalyst.

**Keywords:** Highly dispersed atoms; Targeting strategy; Platinum-based catalyst; Oxygen reduction reaction; Hydrogen evolution reaction.

## 1. Introduction

Oxygen reduction reaction (ORR) and hydrogen evolution reaction (HER) are important components of fuel cells and water splitting [1, 2]. At present, platinum-based catalysts are still the best commercial catalysts for these two reactions. However, platinum is expensive, scarce, and poorly stable limiting its large-scale application [3, 4]. In recent years, sub-nano (single atom, cluster) platinum-supported catalysts have been developed to improve the utilization of platinum [5-7]. However, the catalytic activity of the single-atom active site is greatly affected by the coordination environment of the carrier [8]. Taking ORR catalysis as an example, Li et al. reported a single-atom platinum-supported N-doped carbon catalyst with excellent four-electron selectivity [6]. Song et al. loaded platinum single atoms on another N-doped carbon surface and also showed high four-electron selectivity [9]. While, Kim et al. loaded monoatomic platinum on N-doped carbon, the material exhibited two-electron selectivity and a high hydrogen peroxide yield [10]. Shen et al. loaded platinum single atoms on  $\text{CuS}_x$  also showed high hydrogen peroxide yield [11]. In summary, single-atom platinum-supported catalysts have not yet established a clear structure-performance relationship, and the ORR four-electron catalytic selectivity required by fuel cells cannot be obtained controllably. In addition, the oxidation state of platinum also plays an important role in the catalytic performance [12]. Because single atoms have higher surface energy and activity, they are easy to agglomerate and oxidize [13, 14], which affects the activity and stability of the catalyst. Therefore, improving the dispersibility of platinum to the atomic level cannot obtain the ideal

catalyst with high activity and high stability, and the difficulty of mass production is another important challenge that restricts its application.

In addition to improve the dispersion of platinum atoms on the carrier, introducing cheap transition metal atoms into the platinum lattice to form alloys is another effective strategy to increase the utilization of platinum and reduce the platinum content of the catalyst [15-19]. When platinum is alloyed with transition metals, lattice strain and electronic coordination effects will occur, and the center of the Pt d band will shift, thereby optimizing the bonding strength between platinum and the reactants and improving the performance of the catalyst [20-22]. However, the structural damage caused by the leaching of transition metal elements during use of the platinum alloy catalyst is one of the main problems affecting its stability [23, 24]. In addition, platinum alloy catalysts generally need to be dispersed and supported on a carbon carrier during use. Due to the weak van der Waals force between the alloy particles and the carbon carrier, the nanoparticles are easy to fall off during use and the stability is poor [25]. Therefore, improving the bonding force of platinum alloy and carbon support has research value.

Herein, we used the MOF derivatization strategy to prepare nitrogen-doped porous carbon containing highly dispersed copper atoms. Copper atoms are used as targets loaded by platinum atoms to obtain N-doped porous carbon materials loaded by copper-platinum alloy nanoparticles in one step, which simplifies the loading process of alloy materials. Theoretical calculations show that platinum atoms are more likely to deposit and grow into clusters at copper-containing sites than carbon-nitrogen

structure sites. X-ray photoemission electron microscopy tests show that there is a strong interaction between the carbon support and the CuPt alloy, which improves the stability of the catalyst. The prepared catalyst C-ZIF-CuPt has high activity and high stability to ORR and HER. The platinum mass activity is 4.4 times (ORR) and 6.7 times (HER) of the commercial Pt/C (20 wt%), and its platinum content is only 4.4 wt%. DFT calculations show that copper doping can increase the d-band center of platinum, reduce the ORR overpotential and the activation energy barrier to water molecules, which is beneficial to ORR and HER catalysis. Under the same support conditions, the performance of the sub-nano (single atom, cluster) platinum-supported catalyst (C-ZIF-Cu-Pt) is lower than that of C-ZIF-CuPt. This further shows that platinum alloying can effectively improve the performance of the catalyst.

## **2. Experimental section**

### **2.1. Materials**

Zn(NO<sub>3</sub>)<sub>2</sub>·6H<sub>2</sub>O (AR, Sinopharm Chemical Reagent Co.), Cu(NO<sub>3</sub>)<sub>2</sub>·3H<sub>2</sub>O (99%, Aladdin), 2-methylimidazole (98%, Aladdin), Pt/C (20 wt %, Shanghai Chuxi industrial Co.), chloroplatinic acid (99.9%, Shanghai Boka chem Technology Co.), Al<sub>2</sub>O<sub>3</sub> (fineness: 0.05 μm, Gaoss Union.), KOH (99.99%, Aladdin), N, N-dimethylformamide (DMF) (99.5%, Aladdin), methanol (AR, Sinopharm Chemical Reagent Co.), deionized water (18.25 MΩ·cm resistivity, PSDK water purification system). All materials were directly purchased and used without further processing.

### **2.2. Sample preparation**

*Synthesis of ZIF-8-Cu.* Dissolved 5 mmol  $\text{Zn}(\text{NO}_3)_2 \cdot 6\text{H}_2\text{O}$  and 0.2 mmol  $\text{Cu}(\text{NO}_3)_2 \cdot 3\text{H}_2\text{O}$  in 40 mL methanol, and then dissolved 20 mmol 2-methylimidazole in another 40 mL methanol solution. The two solutions were mixed and stirred for 30 min and then aged at room temperature for 24 h. The product was collected by centrifugation and washed with methanol, and dried under vacuum at 60 °C for 12 h.

*Synthesis of C-ZIF-Cu.* ZIF-8-Cu was placed in a corundum boat and calcined in a tube furnace under a mixed atmosphere of argon (95 v %) and hydrogen (5 v %). The temperature was raised to 950 °C at a rate of 3 °C min<sup>-1</sup> and kept for 2 hours, then naturally cooled to room temperature. The product is labeled C-ZIF-Cu.

*Synthesis of C-ZIF-CuPt.* 8 mg of C-ZIF-Cu was ultrasonically dispersed in 32 mL of deionized water. Under ultrasound, 1200  $\mu\text{L}$  of chloroplatinic acid aqueous solution (3.68 mM) was added, and then the same volume of ascorbic acid aqueous solution (0.1 M) was added. Stop the ultrasound, put the mixed solution in a 65 °C water bath, and keep 4 h. The product was collected by centrifugation and washed three times with water and ethanol, respectively, and dried in vacuum at 60 °C for 12 h.

*Synthesis of C-ZIF-Cu-Pt.* Similar to the preparation method of C-ZIF-CuPt, after adding 1200  $\mu\text{L}$  of chloroplatinic acid aqueous solution, without adding ascorbic acid. The mixed solution was placed in a 65 °C water bath, and keep 4 h. The product was collected by centrifugation and washed three times with water and ethanol, respectively, and dried in vacuum at 60 °C for 12 h.

*Synthesis of C-ZIF-Pt.* Similar to the preparation method of C-ZIF-CuPt, except that it does not contain copper. Dissolve 5 mmol  $\text{Zn}(\text{NO}_3)_2 \cdot 6\text{H}_2\text{O}$  in 40 mL of

methanol and 20 mmol 2-methylimidazole in another 40 mL of methanol solution. The two solutions were mixed and stirred for 30 min and then aged at room temperature for 24 h. The product was collected by centrifugation and washed with methanol, and dried under vacuum at 60 °C for 12 h. The subsequent calcination and platinum loading step is completely consistent with the preparation of C-ZIF-CuPt.

### **2.3. Characterizations**

The crystal phase of the samples was measured by X-ray powder diffraction (XRD, Bruker AXS, D8 Advance using Cu K $\alpha$  radiation). Tested the morphology, element content and distribution of the samples by scanning electron microscopy (SEM, Hitachi, S-8100), transmission electron microscopy (TEM, Hitachi, HT-7700), high resolution transmission electron microscopy (HR-TEM, FEI, Tecnai G220), aberration corrected-high angle annular dark field-scanning transmission electron microscopy (AC-HAADF-STEM, JEOL, JEM-ARM200F), high resolution field emission scanning/transmission electron microscope (HR-STEM, FEI, Talos-F200X). The content of platinum and copper in C-ZIF-CuPt was tested by inductively coupled plasma emission spectrometry (ICP-OES, PerkinElmer, Optima 8000). The Raman spectrum of C-ZIF-Cu was detected using a RENISHAW Raman Microscope equipped with a laser with an excitation wavelength of 532 nm. The surface chemical analysis of the samples was performed by X-ray photoelectron spectroscopy (XPS, Thermo ESCALAB 250XI). The specific surface area and pore size distribution of C-ZIF-Cu was tested by N<sub>2</sub> adsorption/desorption (Micromeritics ASAP 2020). The catalytic performance of the sample was by electrochemical workstation (CHI 760E,

China) and Pine Modulated Speed Rotator (MSR Pine, USA). X-ray photoemission electron microscopy (X-PEEM) based on synchrotron radiation to analyze C k edge of C-ZIF-CuPt. The X-PEEM measurement on this model system was carried out at the PEEM endstation of Beamline MAXPEEM at MAX IV laboratory (Lund, Sweden). For detailed X-PEEM test content, see supporting information.

## **2.4. Electrochemical measurement**

In this electrochemical test, graphite rod is used as the counter electrode, saturated Ag/AgCl electrode is used as the reference electrode, and the working electrode is a glassy-carbon rotating disk electrode (RDE, diameter 5 mm). The glass carbon electrode was polished by  $\text{Al}_2\text{O}_3$ . The catalyst ink was obtained by uniformly dispersing 2 mg samples of Pt/C and 1 mg carbon (Vulcan XC-72) in 665  $\mu\text{L}$  water, 335  $\mu\text{L}$  DMF and 10  $\mu\text{L}$  5% Nafion. Then 20  $\mu\text{L}$  catalyst ink was dropped on the polished glass carbon electrode and dried naturally. The polarization curves of ORR activities were performed in  $\text{O}_2$ -saturated 0.1 M KOH with a scan rate of  $10 \text{ mV s}^{-1}$ , the rotation rate of 1600 rpm, and the background current value of the test under nitrogen saturation conditions was deducted. The cyclic voltammetry curve (CV) of the catalyst was tested under the conditions of 0.1 M KOH  $\text{O}_2$  saturation and  $\text{N}_2$  saturation at a scanning speed of  $20 \text{ mV s}^{-1}$ , respectively. Accelerated durability test (ADT) catalyst ORR stability was carried out by performing 10000 cycles in the potential range of 0.6 to 1.0 V vs RHE in 0.1 M KOH saturated with  $\text{O}_2$  at  $25^\circ\text{C}$ . The HER performance of the catalyst was tested using the same RDE electrode as the ORR test. The polarization curves of HER activities were performed in  $\text{N}_2$ -saturated



0.1 M KOH with a scan rate of 5 mV s<sup>-1</sup> and 1600 rpm. The measured data is compensated for iR. Accelerated durability test (ADT) catalyst HER stability was carried out by performing 1000 cycles in the potential range of -0.1 to 0.3 V vs RHE in 0.1 M KOH saturated with N<sub>2</sub> at 25 °C. Convert the potential reference to a reversible hydrogen electrode (RHE) by the following formula:

$$E \text{ (vs RHE)} = E \text{ (vs Ag/AgCl)} + 0.197 + 0.059 \times \text{pH (0.1 M KOH, pH} \approx 12.8). \quad (1)$$

Rotating ring-disk electrode (RRDE) measurement is similar with RDE measurement except that increases the ring current test. Calculate the peroxide yield and electron transfer number of the catalyst by the following equations (2) and (3), in which I<sub>r</sub>, I<sub>d</sub>, n are individually the ring current, the disk current, the electron transfer number. N is the collection efficiency of the platinum ring, the value is 0.37.

$$\% \text{HO}_2^- = \frac{200I_r/N}{I_d + I_r/N} \quad (2)$$

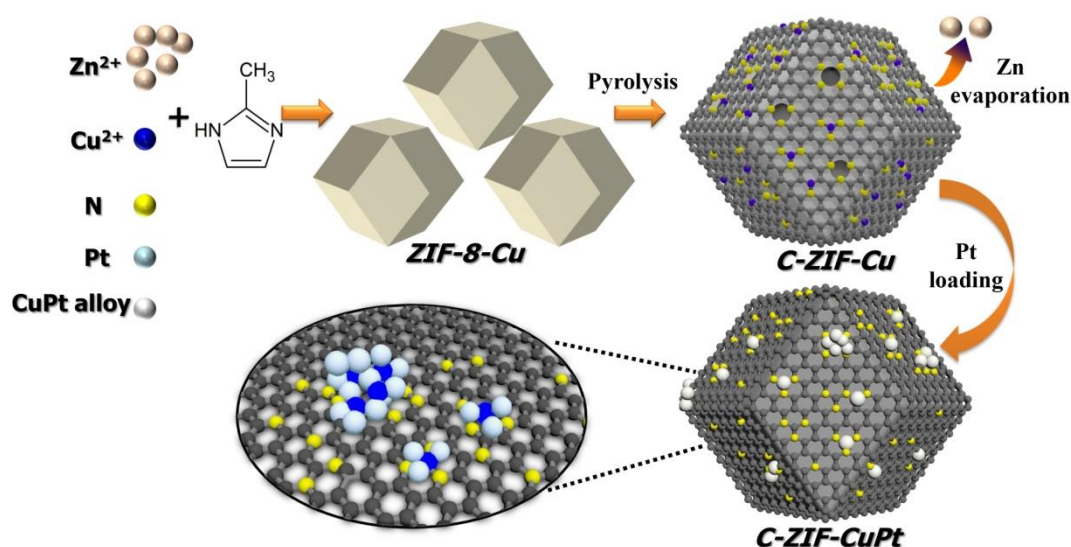
$$n = \frac{4I_d}{I_d + I_r/N} \quad (3)$$

Use the following Koutecky-Levich (K-L) equation to calculate the kinetic current of ORR:

$$\frac{1}{j} = \frac{1}{j_K} + \frac{1}{j_L} = \frac{1}{j_K} + \frac{1}{B\omega^{1/2}} \quad (4)$$

Where *j* is the measured current, *j<sub>K</sub>* is the kinetic current, and *j<sub>L</sub>* is the diffusion limiting current.

### 3. Results and Discussion



**Scheme 1.** C-ZIF-CuPt catalyst preparation process.

The preparation process of C-ZIF-CuPt catalyst is depicted in Scheme 1. The Cu-doped ZIF-8 (ZIF-8-Cu) was first prepared. It owns similar morphology and microstructures as the ZIF-8 as shown in scanning electron microscopic (SEM) images and X-ray diffraction (XRD) patterns in Figure S1. ZIF-8-Cu was calcined at 950 °C in a mixed atmosphere of argon and hydrogen (5 v %). Zinc evaporated (bp: 907 °C) while copper occupied the defects left by zinc volatilization and coordinated with the nitrogen in the material [26]. The N-doped porous carbon material C-ZIF-Cu was obtained. Figure S2 shows its SEM and transmission electron microscope (TEM) images. Elemental mapping (Figure S3b-d) test shows that C, N and Cu are evenly distributed in the material. Spherical aberration correction-high angle circular dark field-scanning transmission electron microscopy (AC-HAADF-STEM) test (Figure S3e, f) denotes a large amount of single atomic Cu dispersions on the sample. As shown in Figure S4, the XRD test showed that during the preparation of the precursor, when the amount of copper nitrate increased from 0.1 mmol to 0.4 mmol, the copper

diffraction peak of the calcined product gradually appeared. This indicates that excessive copper doping will cause copper aggregation during the precursor calcination process, which is not conducive to the dispersion of copper atoms. In order to ensure high dispersion and enough content of copper atoms in the material for the subsequent preparation of copper-platinum alloys, 0.2 mmol copper nitrate is used to prepare the precursor in this work. The nitrogen adsorption and desorption test (Figure S5) shows that C-ZIF-Cu has a large specific surface area and contains a lot of micropores. The Raman spectrum shows that C-ZIF-Cu has a higher degree of graphitization in Figure S6 [27, 28].

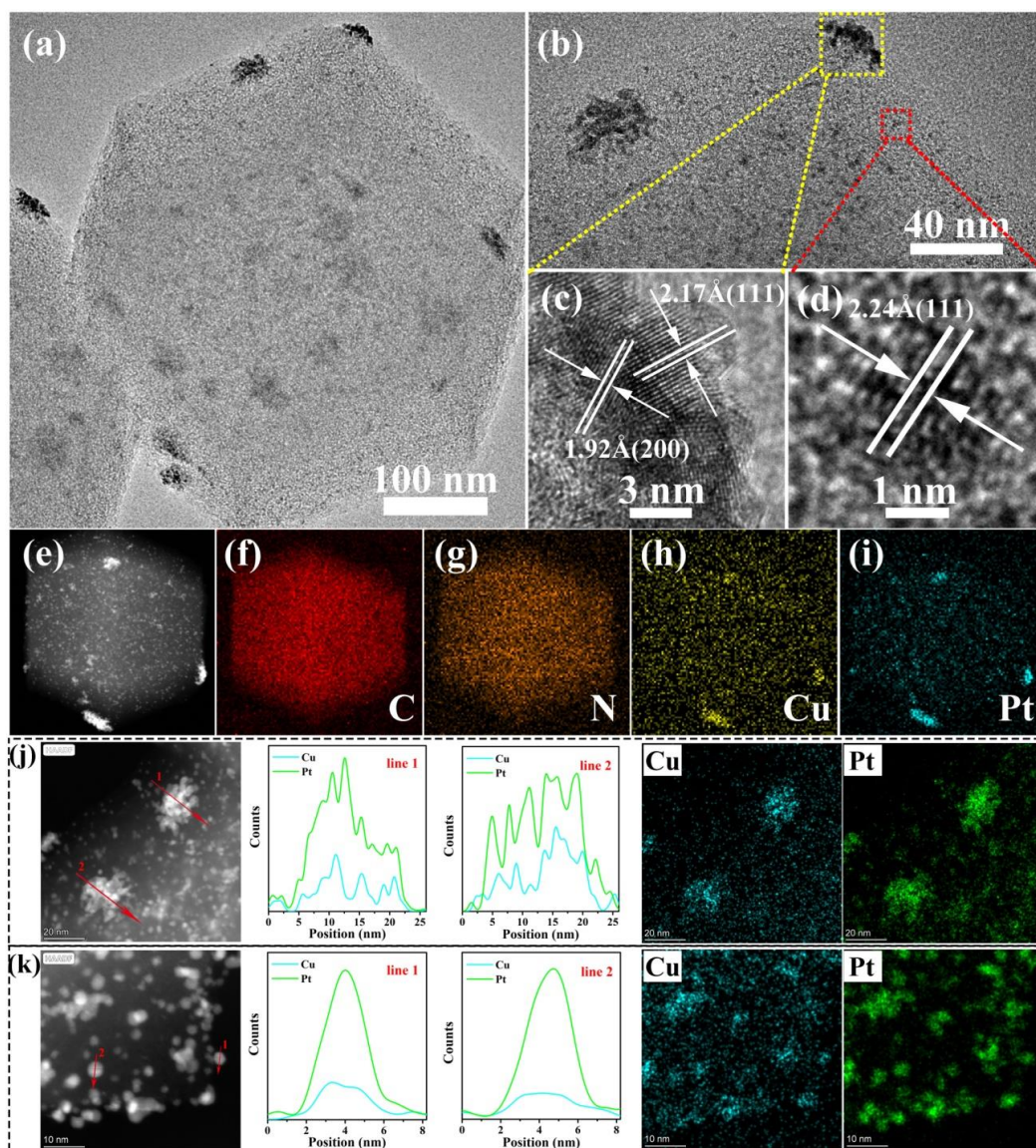


**Figure 1.** (a–d) HR-TEM images of C-ZIF-CuPt. (e–i) HAADF-STEM image of C-ZIF-CuPt and the corresponding C, N, Cu, Pt element mappings, respectively. (j) HAADF-STEM images of C-ZIF-CuPt for CuPt particle accumulation areas, EDS line scan, and Cu, Pt element mappings. (k) HAADF-STEM images of C-ZIF-CuPt for CuPt small nanoparticles areas, EDS line scan, and Cu, Pt element mappings.

The C-ZIF-CuPt alloy materials was obtained by the reduction of chloroplatinic acid with ascorbic acid on C-ZIF-Cu in aqueous solution at 65 °C for 4 hours. As shown in Figure S7, the XRD patterns showed that after the reaction, the peak of

elemental copper disappeared and a wide peak emerged between elemental copper and platinum, indicating that copper atoms were successfully incorporated into the platinum lattice to form a copper-platinum alloy. As shown in Figure 1a-d, the high-resolution transmission electron microscope (HR-TEM) shows that there are a large number of small size nanoparticles and a small number of particle accumulation areas on the surface of the material. The interplanar spacing of the small-sized nanoparticles is 2.24 Å, which is slightly smaller than the (111) crystal plane (2.26 Å) of platinum, illustrating that copper atoms are doped into the platinum lattice, and the radius of copper atoms is smaller than that of platinum, resulting in lattice shrinkage strain and the interplanar spacing decreases [29]. The interplanar spacing of the particle accumulation areas is 2.17 Å, the degree of lattice compression is higher, indicating that the copper content in the accumulation areas is higher. The formation of alloy nanoparticles may be due to the reduction of chloroplatinic acid by ascorbic acid to platinum atoms and deposited on the highly dispersed copper atomic sites on the surface of C-ZIF-Cu, forming copper-platinum alloy. DFT calculations show that compared to carbon and nitrogen sites, platinum atoms are more likely to be supported on copper sites in the carrier to form clusters, which provides a basis for the formation of copper-platinum alloys (See supporting information and Figure S8-9 for calculation details). Since the standard reduction potential  $\text{PtCl}_6^{2+}/\text{Pt}^0$  (0.74 V) is higher than  $\text{Cu}^{2+}/\text{Cu}^0$  (0.34 V) [30], chloroplatinic acid can undergo a substitution reaction with the elemental copper in C-ZIF-Cu. Since C-ZIF-Cu has some copper atom aggregation area, the chloroplatinic acid near this area is reduced by ascorbic

acid on the one hand, and at the same time, the chloroplatinic acid undergoes a substitution reaction with the copper in the matrix, resulting in platinum enrichment in this area. Finally, a unique loose accumulation structure of particles is formed on the surface of the material. The high-angle circular dark-field scanning transmission electron microscope (HAADF-STEM) and element mappings test of a single C-ZIF-CuPt (Figure 1e–i) show that the positional correspondence between copper and platinum is clear, which further proves the formation of the alloy. At the same time, carbon and nitrogen are evenly distributed. In order to further analyze the element distribution in copper-platinum alloy nanoparticles, we selected two sets of particle accumulation areas and small nanoparticles for EDS line scan analysis. As shown in Figure 1j, k, the particle accumulation area and single nanoparticle are both copper-platinum alloys. The sharp fluctuation of the spectrum in the particle accumulation area indicates that the particle structure in the area is rough and the exposed area is large, which is beneficial to catalysis.

Since chloroplatinic acid can undergo a substitution reaction with the elemental copper in C-ZIF-Cu, in addition,  $[\text{PtCl}_6]^{2-}$  can be captured by nitrogen-doped microporous carbon and spontaneously dechlorinated [31]. We do not add the reducing agent ascorbic acid, let chloroplatinic acid react directly with C-ZIF-Cu, and the product is labeled C-ZIF-Cu-Pt. As shown in Figure S10, the surface of C-ZIF-Cu-Pt supports a large number of platinum single atoms and a small number of clusters. The XRD pattern (Figure S7) of C-ZIF-Cu-Pt has no peaks of elemental copper and platinum, which proves the existence of the above reaction process. In

addition, in order to compare with the copper-platinum alloy, we prepared a single-metal platinum supported catalyst by not adding copper ions during the preparation process, and the product was labeled C-ZIF-Pt. The XRD pattern (Figure S7) of C-ZIF-Pt only has a broad elemental platinum peak. The TEM images (Figure S11) shown that the surface of the material is uniformly loaded with platinum nanoparticles with a diameter of about 5 nm, and there is no particle accumulation area. Analyze element composition by energy dispersive spectroscopy (EDS). As shown in Figure S12 and Table S2, the copper content in C-ZIF-Cu-Pt is significantly lower than that in C-ZIF-CuPt, indicating that chloroplatinic acid does indeed undergo a substitution reaction with copper in the substrate. The platinum loadings in C-ZIF-CuPt, C-ZIF-Cu-Pt, and C-ZIF-Pt are similar, which are 3.13 wt %, 3.33 wt %, and 3.24 wt %, respectively.

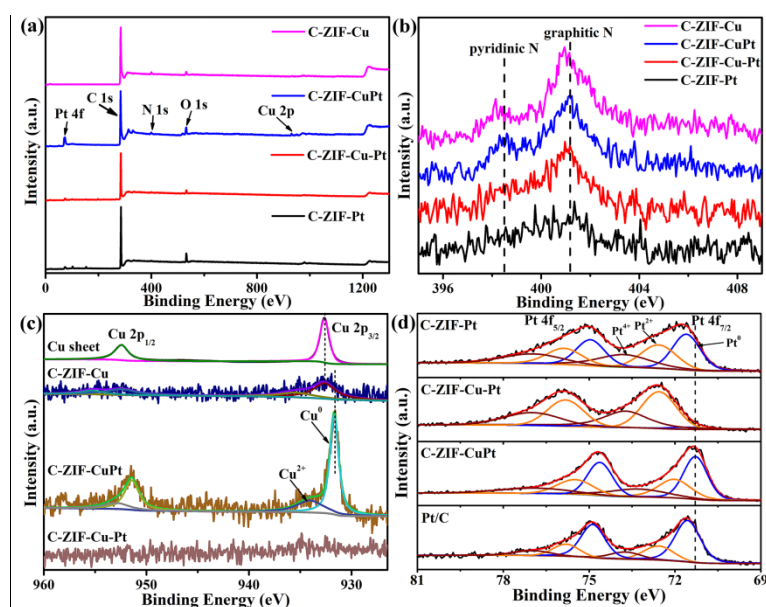


**Figure 2.** (a) XPS spectra of samples. (b) N1s XPS spectra of samples. (c) Cu2p XPS spectra of Cu sheet, C-ZIF-Cu, C-ZIF-CuPt, C-ZIF-Cu-Pt. (d) Pt4f XPS spectra of C-ZIF-Pt, C-ZIF-Cu-Pt, C-ZIF-CuPt, Pt/C (Pt 20 wt %).

In order to study the composition and valence of the elements in the sample, we performed X-ray photoelectron spectroscopy (XPS) test. All spectra are calibrated to 284.8 eV for the C 1s peak. The XPS total spectrum is shown in Figure 2a, and the corresponding element content is shown in Table S3. According to XPS data, the atomic ratio of platinum to copper on the surface of C-ZIF-CuPt is 3:1. According to the ICP-OES test, the platinum and copper contents in C-ZIF-CuPt are 4.41 wt% and 0.48 wt%, respectively. The converted molar ratio is 2.99:1, which is basically consistent with the XPS test result. As shown in Figure 2b, compared with C-ZIF-Cu, the N1s binding energy of the sample is slightly positively shifted after loading platinum, which shows that N interacts with platinum during the platinum loading process and provides electrons to platinum [27, 31]. Figure 2c shows the Cu2p XPS spectrum of the sample, and the fitting results are shown in Table S4. The peaks of C-ZIF-Cu at 932.6 eV and 952.4 eV are Cu<sup>0</sup>2p<sub>3/2</sub> and 2p<sub>1/2</sub>, and there is also a weaker Cu<sup>2+</sup> signal (935.4 eV, 955.3 eV). The Cu2p peak in C-ZIF-CuPt is significantly negatively shifted, and the binding energy of Cu<sup>0</sup>2p<sub>3/2</sub> (931.7 eV) is reduced by 0.9 eV compared with C-ZIF-Cu. This indicates that there is an interaction between copper and platinum. Since the electronegativity of platinum is higher than that of copper, the electrons of copper are transferred to platinum [32-34], resulting in the lack of electrons of copper. This promotes the nitrogen atoms connected to copper to provide electrons to the copper, which in turn leads to the electron enrichment of copper and the reduction of binding energy. At the same time, the Cu signal in C-ZIF-CuPt is significantly stronger than C-ZIF-Cu, and element content analysis shows that the Cu



content on the surface of C-ZIF-CuPt is higher than that of C-ZIF-Cu. This may be due to the substitution reaction between chloroplatinic acid and copper, leading to the leaching of copper in the matrix, which is then reduced by the reducing agent and finally enriched on the surface of the material. Since no reducing agent was added during the preparation of C-ZIF-Cu-Pt, the copper in the matrix reacted with chloroplatinic acid and then was directly lost, resulting in a decrease in surface copper content and disappearance of spectral peaks. In the Pt4f XPS spectrum (Figure 2d), Pt with different chemical valences can be identified, namely  $Pt^0$ ,  $Pt^{2+}$  and  $Pt^{4+}$  [35]. The binding energy and relative peak intensity are shown in Table S5. Compared with Pt/C, the Pt4f peak in C-ZIF-CuPt is negatively shifted by 0.2 eV. This further proves the existence of copper-platinum alloy. The analysis of the Pt4f spectrum in C-ZIF-Cu-Pt shows that the platinum in the material mainly exists in the form of high-valent platinum, which is mainly due to the lack of reducing agent during the preparation process, and zero-valent platinum cannot be effectively generated. In addition, the highly dispersed platinum atoms have higher activity and are easily oxidized to higher chemical states. Since C-ZIF-Pt does not contain copper, chloroplatinic acid is directly reduced by ascorbic acid to form nanoparticles and loaded on the surface of the material. The binding energy of Pt4f is basically the same as that of Pt/C, and the content of platinum oxide is higher than that of Pt/C.

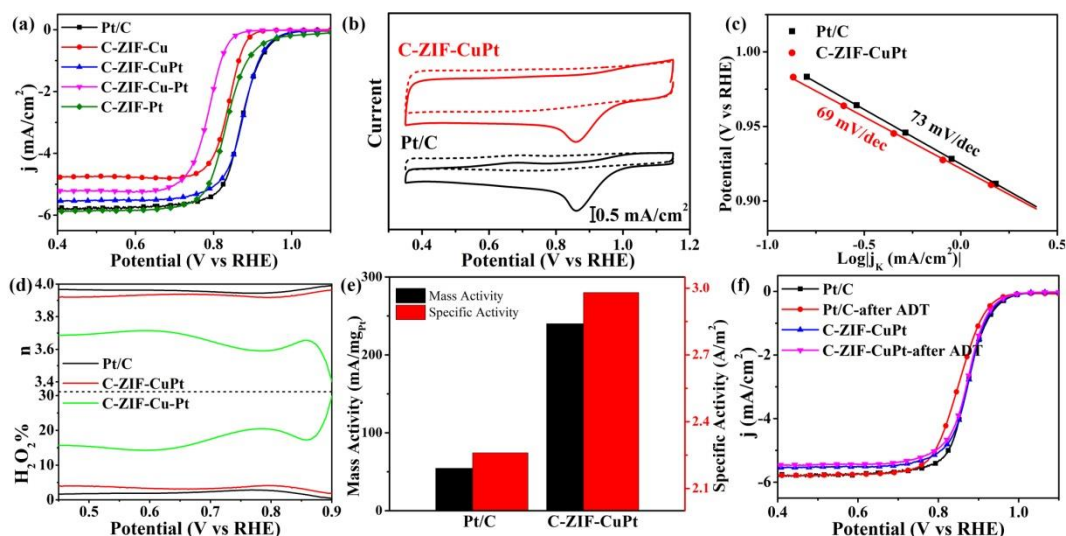


**Figure 3.** (a) ORR polarization curves for catalysts in 0.1 M KOH at 25 °C and 1600 rpm at a scan rate of 10 mV/s. (b) The CV curves of C-ZIF-CuPt and Pt/C are respectively saturated with oxygen (solid line) and saturated with nitrogen (dashed line) at 0.1 M KOH at 25 °C at a scan rate of 20 mV/s. (c) Tafel curve of C-ZIF-CuPt and Pt/C. (d) Calculated  $\text{H}_2\text{O}_2$  yield and transferred electron numbers for C-ZIF-CuPt, C-ZIF-Cu-Pt and Pt/C (20 wt%). (e) The mass activity and specific activity of C-ZIF-CuPt and Pt/C. (f) The ORR polarization curves of C-ZIF-CuPt and Pt/C before and after the ADT test by 10,000 cycles.

As shown in Figure 3a, The ORR catalytic activity of samples were measured by recording the linear sweep voltammetry (LSV) curves on a rotating disk electrode (RDE). The results show that C-ZIF-Cu has a certain ORR catalytic activity, but its performance is poor. After the copper-platinum alloy is formed, the performance of the material is significantly improved. The polarization curve of C-ZIF-CuPt almost overlaps with commercial Pt/C, the half-wave potential is 0.874 V (vs. RHE), and the limiting current density reaches  $5.5 \text{ mA cm}^{-2}$ , which is very close to the performance of Pt/C ( $E_{1/2} = 0.873 \text{ V}$ ,  $J_L = 5.8 \text{ mA cm}^{-2}$ ). In contrast, the half-wave potential and

limiting current density of C-ZIF-Cu-Pt which dispersedly loaded with sub-nano platinum are significantly worse than C-ZIF-CuPt. The highly dispersed platinum atoms on its surface do not exhibit excellent ORR catalytic performance. When the material does not contain copper, the limiting current density of C-ZIF-Pt loaded with platinum nanoparticles is consistent with Pt/C, but the half-wave potential is only 0.835 V, which shows poor catalytic performance. As shown in Figure 3b, the peak potentials in the CV curves of C-ZIF-CuPt and Pt/C are both 0.863 V. Figure 3c, the Tafel slope of C-ZIF-CuPt is less than Pt/C, which indicates that C-ZIF-CuPt has a higher electron transfer rate than Pt/C.

The rotating ring-disk electrode (RRDE) was employed to further explore the catalytic selectivity of materials. According to the RRDE voltammograms shown in Figure S13, the ring current and disc current are substituted into formulas (2) and (3) for calculation to obtain the electron transfer number of catalysts and the hydrogen peroxide yield. As shown in Figure 3b, the electron transfer number of C-ZIF-CuPt is higher than 3.9, the hydrogen peroxide yield is lower than 4%, and the performance is very close to that of Pt/C, indicating that the ORR catalytic selectivity of C-ZIF-CuPt is high. The electron transfer number of C-ZIF-Cu-Pt is less than 3.7, and the hydrogen peroxide yield is above 14%. This shows that the highly dispersed platinum atoms on the surface of C-ZIF-Cu-Pt do not have excellent ORR catalytic selectivity. This is probably related to the high degree of oxidation of platinum atoms on the surface of C-ZIF-Cu-Pt.

The electrochemical active surface area (ECSA) is an important indicator for evaluating catalysts. By testing the CV curve in 0.5 M H<sub>2</sub>SO<sub>4</sub> (Figure S14), the area of the hydrogen desorption zone was calculated and normalized to the platinum loading, and the ECSA of C-ZIF-CuPt and Pt/C were 80.6 m<sup>2</sup>/g<sub>Pt</sub> and 24.1 m<sup>2</sup>/g<sub>Pt</sub>, respectively. The results show that the active area per unit mass of platinum of C-ZIF-CuPt is much higher than that of Pt/C, and the efficiency of platinum is high. The mass activity and specific activity of the catalyst were calculated based on the kinetic current of the ORR at 0.9 V. As shown in Figure 3e, the mass activity of C-ZIF-CuPt is 240.1 mA/mg<sub>Pt</sub>, and the specific activity is 2.98 A/m<sup>2</sup>, which are 4.4 times and 1.3 times that of Pt/C (54.5 mA/mg<sub>Pt</sub>, 2.26 A/m<sup>2</sup>), respectively. Accelerated durability test (ADT) was performed by testing the ORR polarization curve before and after 10,000 cycles of CV. As shown in Figure 3f, the catalytic activity of Pt/C is significantly reduced while the activity of C-ZIF-CuPt is almost unchanged. This indicates that the stability of C-ZIF-CuPt is better than that of Pt/C. As shown in Figure S15, the TEM images of Pt/C before and after the ADT test show that the platinum nanoparticles loaded on carbon are obviously shedding, while the TEM image of C-ZIF-CuPt shows that the copper-platinum alloy particles are stably loaded on the substrate after the ADT test. This shows that the stability of C-ZIF-CuPt is better.

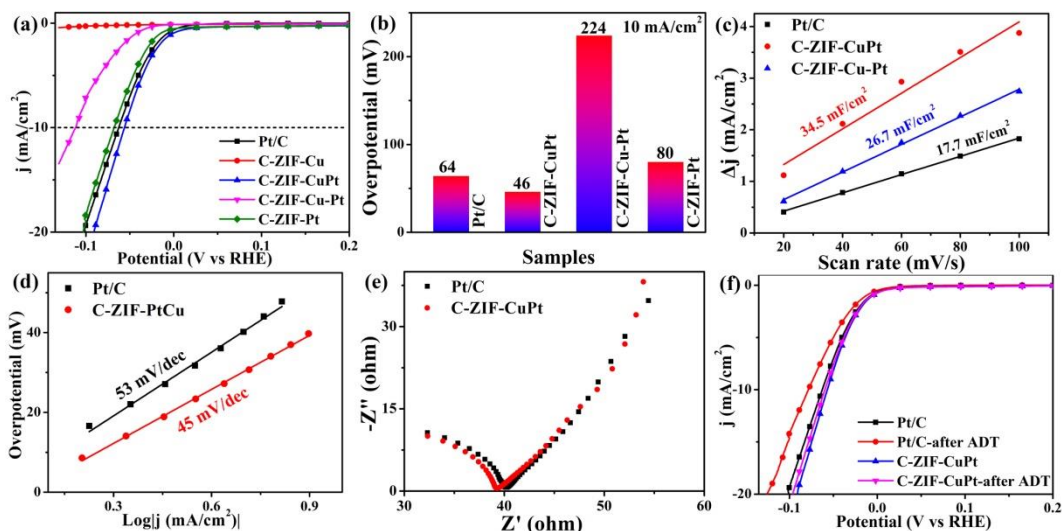


**Figure 4.** (a) HER polarization curves for samples in  $N_2$ -saturated 0.1 M KOH at 25 °C and 1600 rpm at a scan rate of 5 mV/s. (b) Overpotential at 10  $mA/cm^2$  of samples. (c) Capacitive current at 0.14 V (vs RHE) plotted versus scan rate to estimate the 2Cdl of Pt/C, C-ZIF-CuPt and C-ZIF-Cu-Pt. (d) The corresponding Tafel curve of Pt/C and C-ZIF-CuPt obtained from the HER polarization curves in Figure 4a. (e) EIS of Pt/C and C-ZIF-CuPt. (f) The HER polarization curves of C-ZIF-CuPt and Pt/C before and after the ADT test by 1000 cycles.

Under nitrogen saturated conditions, in a 0.1 M KOH solution, the same RDE as ORR was used to test the HER performance of the catalyst. As shown in Figure 4a and b, C-ZIF-Cu has no HER performance. After loading platinum on its surface to form a copper-platinum alloy, its performance has a qualitative leap. C-ZIF-CuPt only needs 46 mV to drive 10  $mA/cm^2$ , which is significantly better than Pt/C (64 mV). The catalytic performance of C-ZIF-Cu-Pt and C-ZIF-Pt are both inferior to that of C-ZIF-CuPt. This shows that in HER catalysis, copper-platinum alloys have advantages over sub-nano-dispersed platinum and single-metal platinum nanoparticles.

The electrochemical active area of the catalyst can be approximated by comparing the

electric double layer capacitance (Cdl) [36]. Figure S16 shows the CV curves of Pt/C, C-ZIF-CuPt and C-ZIF-Cu-Pt at different scanning speeds. Based on the difference between the anode and cathode current density at a potential of 0.14 V and the scanning speed, the slope is twice that of Cdl. As shown in Figure 4c, the 2Cdl value of C-ZIF-CuPt is greater than that of Pt/C and C-ZIF-Cu-Pt. This indicates that C-ZIF-CuPt has a higher electrochemically active area. In Figure 4d, the Tafel slope of C-ZIF-CuPt is lower than Pt/C, indicating that the electron transfer rate of C-ZIF-CuPt is faster. Electrochemical impedance (EIS) is another important parameter to measure catalyst activity. The diameter of the semicircle in the high frequency region in the Nyquist diagram reflects the charge transfer resistance [37]. As shown in Figure 4e, the diameter of the semicircle in the high frequency region of C-ZIF-CuPt is slightly smaller than that of Pt/C, indicating that the electron transfer rate of the material is faster. As shown in Figure 4f, the accelerated durability test is performed through 1000 cycles of CV. The results show that the stability of C-ZIF-CuPt is significantly better than that of Pt/C. In addition, as shown in Figure S17, C-ZIF-CuPt showed a mass activity of 541.4 mA/mg<sub>Pt</sub> in HER catalysis at an overpotential of 0.3 mV, which was 6.7 times that of Pt/C (80.9 mA/mg<sub>Pt</sub>). This shows that the platinum utilization rate in C-ZIF-CuPt is significantly higher than that of Pt/C.

In order to optimize platinum loading in C-ZIF-CuPt on the catalytic performance of the material, we controlled the chloroplatinic acid content in the preparation process of C-ZIF-CuPt to be between 200  $\mu$ L and 1400  $\mu$ L. As shown in Figure S18,

when the amount of chloroplatinic acid is 1200  $\mu\text{L}$ , the material has the best ORR and HER dual-functional catalytic performance. In addition, we also compared the effects of substrates with different copper content on the structure and performance of the material. As shown in Figure S19a-d, when the  $\text{Cu}(\text{NO}_3)_2 \cdot 3\text{H}_2\text{O}$  used in the preparation of the precursor is 0.1 mmol, the copper atoms in the calcined product are highly dispersed, and the XRD spectrum (Figure S4) does not have the peak of elemental copper. After platinum is loaded, fine nanoparticles are formed on the surface of the material. When the amount of  $\text{Cu}(\text{NO}_3)_2 \cdot 3\text{H}_2\text{O}$  is 0.4 mmol, the copper atoms in the calcined product aggregate, and the XRD spectrum shows obvious elemental copper peaks in Figure S4. After platinum is loaded, a large number of particle accumulation areas are formed on the surface of the material. This phenomenon further proves that the morphology of the copper-platinum alloy on the surface of the material is related to the dispersed state of copper atoms in the material. As shown in Figure S19e and f, higher or lower copper content of the substrate shows poor ORR and HER catalytic performance. When the amount of  $\text{Cu}(\text{NO}_3)_2 \cdot 3\text{H}_2\text{O}$  is 0.2 mmol, the material has the best catalytic performance.

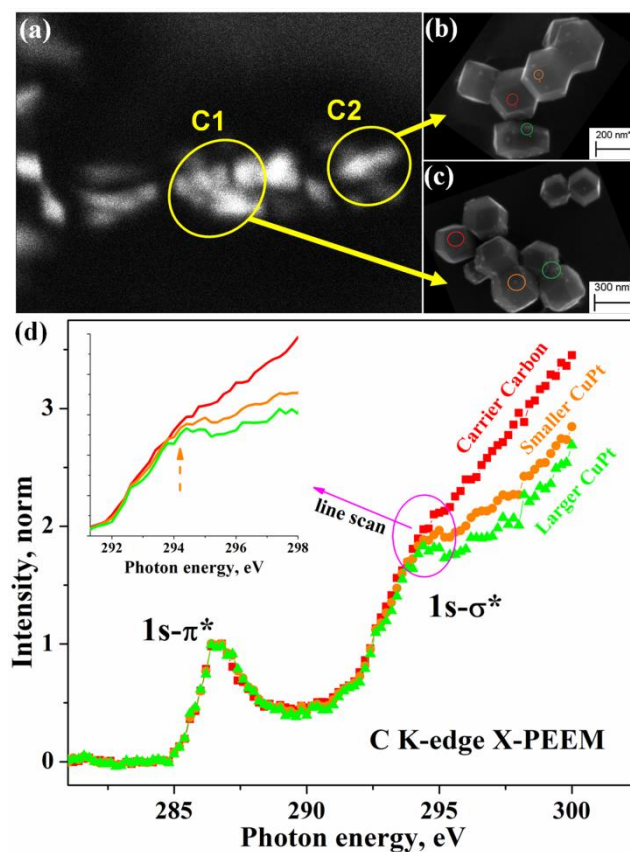


**Figure 5.** (a) Original X-PEEM view of C-ZIF-CuPt. (b, c) are the SEM images of areas C2 and C1 in Figure 5a. (d) C K-edge x-ray absorption spectra of selected sites at C1 as shown in different color circles as red for bare carrier carbon, orange for smaller CuPt clusters and green circle corresponds larger CuPt particles on carrier, respectively.

The bonding conditions between the copper-platinum alloy and the carrier were investigated through the microregional C k-edge x-ray absorption spectra (XAS) of C-ZIF-CuPt recorded on an X-ray photoemission electron microscope (X-PEEM). Figure 5a depicts an actual X-PEEM image of the probed local sites of C-ZIF-CuPt dispersed on a Si wafer with its parts zoomed in SEM images labelled as C2, C1 in Figure 5b, c. The same SEM images were amplified in Figure S20 for clarifications of particle sizes. In each area, three different local sites with the same area have been



chosen for the analysis. Red circle indicates the bare carrier carbon, orange and green ones correspond to smaller and larger CuPt clusters or particles on carrier carbon surfaces, respectively. Figure 5d shows the comparative plot of corresponding spectra at area C1 for red, orange and green circles as from bare carrier carbon, smaller CuPt and larger CuPt sites, respectively. As shown in Figure 5d, the feature in the energy range 285 to 290 eV typically refers to C 1s  $\rightarrow \pi^*$  transition while the latter feature up to 300 eV to be due to C 1s  $\rightarrow \sigma^*$  transition. On comparing the spectra, one can clearly observe the spectroscopic differences, which is significant near  $\sigma^*$  states. The differences are visible in other areas such as C2 as given in Figure S21 for the similar regions of interests. By comparing the first three spectra, at the position indicated by the purple arrow, the shoulder peak feature shapes more into peak like from no CuPt to larger CuPt clusters. Such change in XAS spectra suggest the presence of new electronic states in the conduction band derived from hybridization of C- $\pi/\sigma$  network with Cu and Pt d-orbitals [38-40]. In the Figure 5d, suppressed intensity of unoccupied  $\sigma^*$  states of C happens, possibly due to electron transfer between metallic orbitals and C-2p. The PEEM-XAS data indicate that the C carrier exhibits a strong orbital interaction with the CuPt particles. Such an interaction is weaker with smaller ones which are mostly due to Pt's oxidizations therein as given in the XPS analysis. The interaction is constructive to the firm loading of CuPt on the surface of the carbon matrix, retain chemical activities of the CuPt, and improving the stability of the composites.

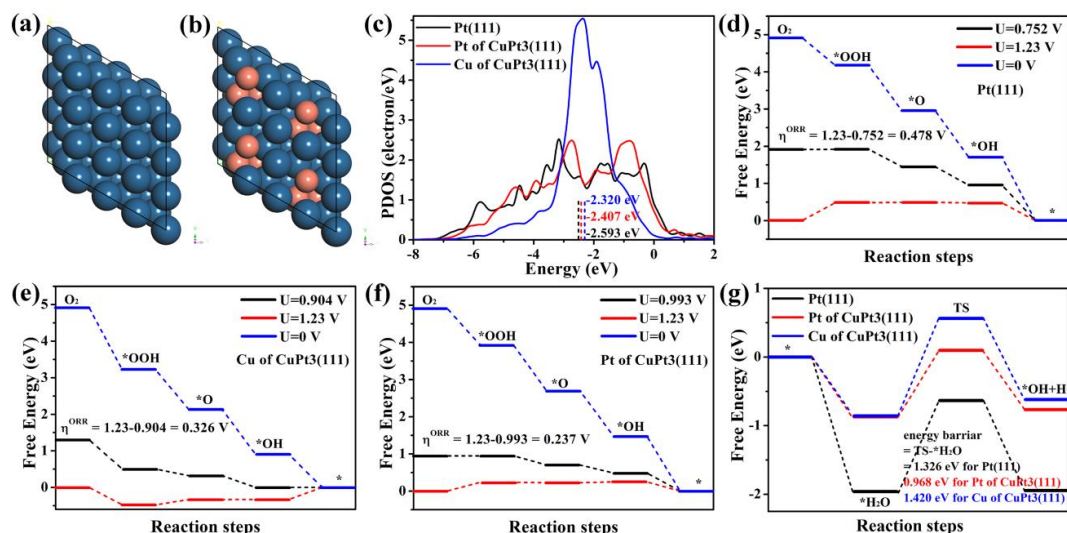


**Figure 6.** Models of (a) Pt(111) and (b) CuPt<sub>3</sub>(111). The blue ball represents Pt, and the brick red ball represents Cu. (c) PDOS of d orbitals of Pt(111) and CuPt<sub>3</sub>(111). The calculated d-band centers are marked with dotted lines. (d-f) The free energy path of ORR on the surface of Pt(111), Cu and Pt sites of CuPt<sub>3</sub>(111), respectively. (g) The activation energy barriers of H<sub>2</sub>O molecules in the HER of three model structures.

The influence of copper-platinum alloy structure on catalytic performance was studied by using DFT calculation. A model of CuPt<sub>3</sub>(111) was constructed according to the XPS determination on element abundance and compared with Pt(111) as shown in Figure 6a and 6b. The d-band centers of the systems are also given in Figure 6c with its computational method in SI. Results show that the d band center of copper in CuPt<sub>3</sub> is closest to the Fermi level, followed by the platinum site of CuPt<sub>3</sub>(111), and the platinum site of Pt(111), which are -2.320, -2.407 and -2.593 eV, respectively. Figure 6d-f present the free energy paths of the ORR at different potentials at three different configuration sites. The intermediates adsorption configuration is depicted in Figure S22. The results show that the overpotential of ORR at the platinum site of Pt(111) is 0.478 V. After the copper-platinum alloy is formed, the overpotential of

platinum in the copper-platinum alloy is 0.237 V, and the overpotential of copper is 0.326 V. The doping of copper significantly reduces the ORR overpotential of the Pt active site, and promotes the ORR catalytic performance of the material. Under alkaline conditions, the key to the reaction rate of HER is the activation energy of water molecules (the energy barrier for the decomposition of  $\text{H}_2\text{O}$  into  $\text{OH}+\text{H}$ ) [41, 42]. As shown in Figure 6g, the water decomposition energy barrier of the platinum site of the copper-platinum alloy is 0.958 eV, which is significantly lower than pure platinum (1.326 eV). The corresponding intermediate adsorption configuration is shown in Figure S23. Copper doping effectively reduces the activation energy barrier of platinum to water molecules, which enables excellent HER performance on C-ZIF-CuPt.

#### **4. Conclusion**

In summary, we disperse and support copper atoms on the carrier in advance, then use them as platinum-supported targets, and finally directionally support platinum atoms to obtain a copper-platinum alloy-supported nitrogen-doped porous carbon material. The method simplifies the preparation and loading process of platinum alloy materials. In addition, because copper atoms are embedded on the nitrogen-doped carbon support, it is beneficial for the copper-platinum alloy nanoparticles to be firmly anchored on the support, and the stability of the catalyst is improved. The X-PEEM test results confirmed the strong orbital interaction between the carrier carbon and the copper-platinum alloy. The ORR performance of the obtained catalyst

C-ZIF-CuPt is equivalent to that of Pt/C, and the HER performance is better than that of Pt/C. Its platinum mass activity is 4.4 times (ORR) and 6.7 times (HER) of commercial Pt/C (20 wt%), and its platinum content is only 4.4 wt%. The accelerated durability test shows that the stability of the catalyst is significantly better than that of Pt/C. DFT calculations show that Cu doping can increase the d-band center of Pt, reduce the ORR overpotential and the activation energy barrier to water molecules, thereby improving the ORR and HER catalytic performance of the material. In addition, under the same loading conditions, the sub-nanoscale (single atom, cluster) dispersed platinum supported catalyst C-ZIF-Cu-Pt showed poor ORR selectivity and HER catalytic performance. This further shows that platinum alloying can effectively improve the performance of the catalyst.

### **Declaration of Competing Interest**

The author declares that there are no known competing financial interests or personal relationships that may affect the work reported in this article.

### **Acknowledgements**

This work was supported by the National Natural Science Foundation of China (21871005), the Program for Innovative Research Team of Anhui Education Committee, the Project for Collaborative Innovation of Anhui Higher Education Institutes (GXXT-2020-005). The authors thank also the crew of the MAX IV laboratory for their support during the beamtime operation.

## Appendix A. Supplementary date

This Supplementary date associated with this article can be found, in the online version, at [http: http://dx.doi.org/xxx](http://dx.doi.org/xxx).

## References

- [1] X. S. Lv, W. Wei, H. Wang, B. B. Huang, Y. Dai, Multifunctional electrocatalyst PtM with low Pt loading and high activity towards hydrogen and oxygen electrode reactions: A computational study, *Appl Catal B-Environ*, 255 (2019) 117743.
- [2] H. T. Lei, X. L. Li, J. Meng, H. Q. Zheng, W. Zhang, R. Cao, Structure Effects of Metal Corroles on Energy-Related Small Molecule Activation Reactions, *Acs Catal*, 9 (2019) 4320-4344.
- [3] J. Y. Park, D. H. Kwak, K. B. Ma, S. B. Han, G. S. Chai, S. K. Kim, D. H. Peck, C. S. Kim, A. Kucernak, K. W. Park, Enhanced oxygen reduction reaction of Pt deposited Fe/N-doped bimodal porous carbon nanostructure catalysts, *J Catal*, 359 (2018) 46-54.
- [4] M. X. Gong, D. D. Xiao, Z. P. Deng, R. Zhang, W. W. Xia, T. H. Zhao, X. P. Liu, T. Shen, Y. Z. Hu, Y. Lu, X. Zhao, H. L. Xin, D.L. Wang, Structure evolution of PtCu nanoframes from disordered to ordered for the oxygen reduction reaction, *Appl Catal B-Environ*, 282 (2021) 119617.
- [5] H. E. Kim, I. H. Lee, J. Cho, S. Shin, H. C. Ham, J. Y. Kim, H. Lee, Palladium Single-Atom Catalysts Supported on C@C<sub>3</sub>N<sub>4</sub> for Electrochemical Reactions, *Chemelectrochem*, 6 (2019) 4757-4764.

- [6] T. F. Li, J. J. Liu, Y. Song, F. Wang, Photochemical Solid-Phase Synthesis of Platinum Single Atoms on Nitrogen-Doped Carbon with High Loading as Bifunctional Catalysts for Hydrogen Evolution and Oxygen Reduction Reactions, *Acs Catal*, 8 (2018) 8450-8458.
- [7] J. Liu, J. Bak, J. Roh, K.S. Lee, A. Cho, J.W. Han, E. Cho, Reconstructing the Coordination Environment of Platinum Single-Atom Active Sites for Boosting Oxygen Reduction Reaction, *Acs Catal*, 11 (2021) 466-475.
- [8] B. Zhang, G. Sun, S. P. Ding, H. Asakura, J. Zhang, P. Sautet, N. Yan, Atomically Dispersed Pt-1-Polyoxometalate Catalysts: How Does Metal-Support Interaction Affect Stability and Hydrogenation Activity?, *J Am Chem Soc*, 141 (2019) 8185-8197.
- [9] Z. X. Song, Y. N. Zhu, H. S. Liu, M. N. Banis, L. Zhang, J. J. Li, K. Doyle-Davis, R.Y. Li, T. K. Sham, L. J. Yang, A. Young, G. A. Botton, L. M. Liu, X. L. Sun, Engineering the Low Coordinated Pt Single Atom to Achieve the Superior Electrocatalytic Performance toward Oxygen Reduction, *Small*, (2020) 2003096.
- [10] J. H. Kim, D. Shin, J. Lee, D. S. Baek, T. J. Shin, Y. T. Kim, H. Y. Jeong, J. H. Kwak, H. Kim, S. H. Joo, A General Strategy to Atomically Dispersed Precious Metal Catalysts for Unravelling Their Catalytic Trends for Oxygen Reduction Reaction, *Acs Nano*, 14 (2020) 1990-2001.
- [11] R. G. Shen, W. X. Chen, Q. Peng, S. Q. Lu, L. R. Zheng, X. Cao, Y. Wang, W. Zhu, J. T. Zhang, Z. B. Zhuang, C. Chen, D. G. Wang, Y. D. Li, High-Concentration

Single Atomic Pt Sites on Hollow CuS<sub>x</sub> for Selective O<sub>2</sub> Reduction to H<sub>2</sub>O<sub>2</sub> in Acid Solution, *Chem-US*, 5 (2019) 2099-2110.

[12] S. Shin, J. Kim, S. Park, H.E. Kim, Y.E. Sung, H. Lee, Changes in the oxidation state of Pt single-atom catalysts upon removal of chloride ligands and their effect for electrochemical reactions, *Chem Commun*, 55 (2019) 6389-6392.

[13] Y. J. Chen, S. F. Ji, C. Chen, Q. Peng, D. S. Wang, Y. D. Li, Single-Atom Catalysts: Synthetic Strategies and Electrochemical Applications, *Joule*, 2 (2018) 1242-1264.

[14] B. W. Zhang, Y. X. Wang, S. L. Chou, H. K. Liu, S. X. Dou, Fabrication of Superior Single-Atom Catalysts toward Diverse Electrochemical Reactions, *Small Methods*, 3 (2019) 1800497.

[15] C. A. Campos-Roldan, L. Calvillo, G. Granozzi, N. Alonso-Vante, Alkaline hydrogen electrode and oxygen reduction reaction on Pt<sub>x</sub>Ni nanoalloys, *J Electroanal Chem*, 857 (2020) 113449.

[16] X. X. Zhu, L. Huang, M. Wei, P. Tsiakaras, P. K. Shen, Highly stable Pt-Co nanodendrite in nanoframe with Pt skin structured catalyst for oxygen reduction electrocatalysis, *Appl Catal B-Environ*, 281 (2021) 119460.

[17] M. A. Matin, J. Lee, G. W. Kim, H. U. Park, B. J. Cha, S. Shastri, G. Kim, Y. D. Kim, Y.U. Kwon, V. Petkov, Morphing Mn-core@Pt-shell nanoparticles: Effects of core structure on the ORR performance of Pt shell, *Appl Catal B-Environ*, 267 (2020) 118727.

- [18] X. R. Zhao, C. Xi, R. Zhang, L. Song, C. Y. Wang, J. S. Spendelow, A. I. Frenkel, J. Yang, H. L. Xin, K. Sasaki, High-Performance Nitrogen-Doped Intermetallic PtNi Catalyst for the Oxygen Reduction Reaction, *Acs Catal*, 10 (2020) 10637-10645.
- [19] Y. X. Xie, Y. Yang, D. A. Muller, H. D. Abruna, N. Dimitrov, J. Y. Fang, Enhanced ORR Kinetics on Au-Doped Pt-Cu Porous Films in Alkaline Media, *Acs Catal*, 10 (2020) 9967-9976.
- [20] N. K. Chaudhari, J. Joo, H. B. Kwon, B. Kim, H. Y. Kim, S. H. Joo, K. Lee, Nanodendrites of platinum-group metals for electrocatalytic applications, *Nano Res*, 11 (2018) 6111-6140.
- [21] P. Strasser, S. Koh, T. Anniyev, J. Greeley, K. More, C. F. Yu, Z. C. Liu, S. Kaya, D. Nordlund, H. Ogasawara, M. F. Toney, A. Nilsson, Lattice-strain control of the activity in dealloyed core-shell fuel cell catalysts, *Nat Chem*, 2 (2010) 454-460.
- [22] X. R. Zhao, H. Cheng, L. Song, L. L. Han, R. Zhang, G. H. Kwon, L. Ma, S. N. Ehrlich, A. I. Frenkel, J. Yang, K. Sasaki, H. L. Xin, Rhombohedral Ordered Intermetallic Nanocatalyst Boosts the Oxygen Reduction Reaction, *Acs Catal*, 11 (2021) 184-192.
- [23] N. K. Chaudhari, J. Joo, B. Kim, B. Ruqia, S. I. Choi, K. Lee, Recent advances in electrocatalysts toward the oxygen reduction reaction: the case of PtNi octahedra, *Nanoscale*, 10 (2018) 20073-20088.



- [24] C. H. Cui, L. Gan, M. Heggen, S. Rudi, P. Strasser, Compositional segregation in shaped Pt alloy nanoparticles and their structural behaviour during electrocatalysis, *Nat Mater*, 12 (2013) 765-771.
- [25] D. Wang, Q. Y. Wang, S. D. Jiang, K. Z. Dong, Z. Y. Wang, S. H. Luo, Y. G. Liu, Y. H. Zhang, Q. Wang, T. F. Yi, NiCo alloy nanoparticles encapsulated in N-doped 3D porous carbon as efficient electrocatalysts for oxygen reduction reaction, *Int J Hydrogen Energ*, 45 (2020) 22797-22807.
- [26] S. H. Ma, Z. Han, K. Y. Leng, X. J. Liu, Y. Wang, Y. T. Qu, J. B. Bai, Ionic Exchange of Metal-Organic Frameworks for Constructing Unsaturated Copper Single-Atom Catalysts for Boosting Oxygen Reduction Reaction, *Small*, 16 (2020) 2001384.
- [27] C. Wang, X. D. Wang, F. Y. Lai, Z. Liu, R. H. Dong, W. Li, H. X. Sun, B. Y. Geng, Pt Nanoparticles Supported on N-Doped Porous Carbon Derived from Metal-Organic Frameworks for Oxygen Reduction, *Acs Appl Nano Mater*, 3 (2020) 5698-5705.
- [28] A. Sadezky, H. Muckenhuber, H. Grothe, R. Niessner, U. Poschl, Raman micro spectroscopy of soot and related carbonaceous materials: Spectral analysis and structural information, *Carbon*, 43 (2005) 1731-1742.
- [29] N. K. Chaudhari, Y. Hong, B. Kim, S. I. Choi, K. Lee, Pt-Cu based nanocrystals as promising catalysts for various electrocatalytic reactions, *J Mater Chem A*, 7 (2019) 17183-17203.

- [30] P. Li, C. Du, X. H. Gao, Z. H. Zhuang, D. Xiang, C. M. Zhang, W. Chen, Insights into the morphology and composition effects of one-dimensional CuPt nanostructures on the electrocatalytic activities and methanol oxidation mechanism by in situ FTIR, *Nanoscale*, 12 (2020) 13688-13696.
- [31] Z. Q. Zhang, Y. G. Chen, L. Q. Zhou, C. Chen, Z. Han, B. S. Zhang, Q. Wu, L. J. Yang, L. Y. Du, Y. F. Bu, P. Wang, X. Z. Wang, H. Yang, Z. Hu, The simplest construction of single-site catalysts by the synergism of micropore trapping and nitrogen anchoring, *Nat Commun*, 10 (2019) 1657.
- [32] Y. X. Du, K. Ni, Q. X. Zhai, Y. P. Yun, Y. J. Xu, H. T. Sheng, Y. W. Zhu, M. Z. Zhu, Facile air oxidative induced dealloying of hierarchical branched PtCu nanodendrites with enhanced activity for hydrogen evolution, *Appl Catal a-Gen*, 557 (2018) 72-78.
- [33] M. X. Gong, G. T. Fu, Y. Chen, Y. W. Tang, T. H. Lu, Autocatalysis and Selective Oxidative Etching Induced Synthesis of Platinum-Copper Bimetallic Alloy Nanodendrites Electrocatalysts, *Acs Appl Mater Inter*, 6 (2014) 7301-7308.
- [34] Y. G. Zhao, J. J. Liu, C. G. Liu, F. Wang, Y. Song, Amorphous CuPt Alloy Nanotubes Induced by Na<sub>2</sub>S<sub>2</sub>O<sub>3</sub> as Efficient Catalysts for the Methanol Oxidation Reaction, *Acs Catal*, 6 (2016) 4127-4134.
- [35] Y. Dong, Y. W. Zhou, M. Z. Wang, S. L. Zheng, K. Jiang, W. B. Cai, Facile Aqueous Phase Synthesis of Carbon Supported B-doped Pt<sub>3</sub>Ni Nanocatalyst for Efficient Oxygen Reduction Reaction, *Electrochim Acta*, 246 (2017) 242-250.

- [36] X. Zhong, L. Wang, Z. Z. Zhuang, X. L. Chen, J. Zheng, Y. L. Zhou, G. L. Zhuang, X. N. Li, J. G. Wang, Double Nanoporous Structure with Nanoporous PtFe Embedded in Graphene Nanopores: Highly Efficient Bifunctional Electrocatalysts for Hydrogen Evolution and Oxygen Reduction, *Adv Mater Interfaces*, 4 (2017) 1601029.
- [37] Q. Bai, F. C. Shen, S. L. Li, J. Liu, L. Z. Dong, Z. M. Wang, Y. Q. Lan, Cobalt@Nitrogen-Doped Porous Carbon Fiber Derived from the Electrospun Fiber of Bimetal-Organic Framework for Highly Active Oxygen Reduction, *Small Methods*, 2 (2018) 1800049.
- [38] W. J. Huang, H. T. Wang, J. G. Zhou, J. Wang, P. N. Duchesne, D. Muir, P. Zhang, N. Han, F. P. Zhao, M. Zeng, J. Zhong, C. H. Jin, Y. G. Li, S. T. Lee, H. J. Dai, Highly active and durable methanol oxidation electrocatalyst based on the synergy of platinum-nickel hydroxide-graphene, *Nat Commun*, 6 (2015) 10035.
- [39] H. Fukidome, M. Kotsugi, K. Nagashio, R. Sato, T. Ohkochi, T. Itoh, A. Toriumi, M. Suemitsu, T. Kinoshita, Orbital-specific Tunability of Many-Body Effects in Bilayer Graphene by Gate Bias and Metal Contact, *Sci Rep-Uk*, 4 (2014) 4713.
- [40] V. Lee, C. Park, C. Jaye, D. A. Fischer, Q. K. Yu, W. Wu, Z.H. Liu, S. S. Pei, C. Smith, P. Lysaght, S. Banerjee, Substrate Hybridization and Rippling of Graphene Evidenced by Near-Edge X-ray Absorption Fine Structure Spectroscopy, *J Phys Chem Lett*, 1 (2010) 1247-1253.

- [41] J. Yin, J. Jin, H. Zhang, M. Lu, Y. Peng, B. L. Huang, P. X. Xi, C. H. Yan, Atomic Arrangement in Metal-Doped NiS<sub>2</sub> Boosts the Hydrogen Evolution Reaction in Alkaline Media, *Angew Chem Int Edit*, 58 (2019) 18676-18682.
- [42] B. Z. Lu, L. Guo, F. Wu, Y. Peng, J. E. Lu, T. J. Smart, N. Wang, Y. Z. Finfrock, D. Morris, P. Zhang, N. Li, P. Gao, Y. Ping, S. W. Chen, Ruthenium atomically dispersed in carbon outperforms platinum toward hydrogen evolution in alkaline media, *Nat Commun*, 10 (2019) 631.